ELSEVIER

Nuclear Physics A 600 (1996) 37–62

NUCLEAR PHYSICS A

Effects of E2 transitions in the Coulomb dissociation of ^{8}B

H. Esbensen [a], G.F. Bertsch [b]

[a] *Physics Division, Argonne National Laboratory, Argonne, IL 60439, USA*

[b] *Institute of Nuclear Theory, and Department of Physics, FM-15, University of Washington, Seattle, WA 98195, USA*

Received 6 October 1995; revised 20 December 1995

Abstract

We examine the Coulomb dissociation of ^{8}B in a model that has both E1 and E2 matrix elements. We find that the interference between E1 and E2 amplitudes produces large asymmetries in the angular and momentum distributions of the emitted protons and ^{7}Be fragments. By measuring these asymmetries one may be able to put constraints on the E2 component and thereby improve the accuracy of the E1 strength that can be extracted from Coulomb dissociation experiments. We also investigate the effect of higher-order dynamical processes and find that they reduce the asymmetries in reactions on high-Z targets. They also reduce the effect of E2 transitions on the dissociation probability and on the peak height of the decay energy spectrum compared to predictions of first-order perturbation theory.

1. Introduction

Coulomb excitation is a powerful tool to study electromagnetic transition matrix elements, and is now being applied to reactions of astrophysical interest. In particular, Motobayashi et al. [1] inferred the capture cross section for ^{7}Be+p$\rightarrow^8$B+γ from the inverse breakup reaction, ^{8}B$\rightarrow^7$Be+p, induced by Coulomb excitation.

Unfortunately, the information provided by the inverse cross section is not complete, because electromagnetic multipoles contribute with different strengths in capture and in Coulomb excitation. The capture reaction at stellar temperatures is completely dominated by the dipole transition, but the Coulomb excitation cross section has a non-negligible contribution from the electric quadrupole operator. Thus the capture cross section cannot be accurately determined without an independent measurement of the E2 matrix elements. This has in fact led to controversy on the interpretation of the Motobayashi

SSDI 0375-9474(96)00006-1

experiment, with Ref. [2] claiming that E2 transitions contribute as much as 25% to the measured Coulomb excitation. In principle, the angular distribution of the ^{7}Be+p final state depends on the interference of different multipoles and thus can provide an additional constraint on the relative contributions of E1 and E2. Our object in this paper is to explore in detail the role of the E2 amplitude in the angular distribution and in the total cross section.

There are too many independent amplitudes to study this purely phenomenologically, so we will examine the reaction in the framework of a model that has both E2 and E1 matrix elements. We will find that the angular distribution of the emitted proton is rather sensitive to the E2 interference. This result was already reported in a recent letter [3]. We also find that higher-order E1 amplitudes have comparable effects, but of the opposite sign. Because of the cancellation, the E2 effects are smaller than first supposed.

In the next section, we describe our model of ^{8}B. The general formulas for first-order Coulomb excitation are given in Section 3, and the application to angular distributions is discussed in Section 4. Section 5 gives some numerical results, and Section 6 extends the results to higher order in the external Coulomb field.

2. Single-particle model

To study the Coulomb dissociation, $^8\mathrm{B} \rightarrow ^7\mathrm{Be} + \mathrm{p}$, we shall use a simple single-particle description of the loosely bound valence proton. The parameters of the model of course need to be fixed by the properties of the ground state, which we first mention.

2.1. The ground state of ^{8}B

The ground state is a 2^+ state with a proton separation energy of 137 keV. Shell-model calculations [4] show that there are only three configurations of the ground state which involve a weakly bound proton coupled to a low-lying state in ^{7}Be, and these are the most important configurations for the low-energy Coulomb dissociation, $^8\mathrm{B}+\gamma \rightarrow ^7\mathrm{Be}+\mathrm{p}$, and radiative capture, $^7\mathrm{Be}+\mathrm{p} \rightarrow ^8\mathrm{B}+\gamma$.

The most important configuration is a $p_{3/2}$ proton coupled to the $3/2^-$ ground state of ^{7}Be, forming a $J = 2^+$ ground state. The spectroscopic amplitude for this configuration is 0.9884, and it is the one that dominates low-lying E1 transitions. To get realistic M1 transitions it is also important to include a $p_{1/2}$ proton coupled to the ^{7}Be ground state. The spectroscopic amplitude for this configuration is -0.2364. There is only one additional configuration which involves a weakly bound p-wave proton, namely a $p_{3/2}$ proton coupled to the $1/2^-$ excited state of ^{7}Be at 0.429 MeV; it has the spectroscopic amplitude 0.4303. In the following we assume for simplicity that the 2^+ ground state of ^{8}B can be described as a $p_{3/2}$ proton wave coupled to the $3/2^-$ ground state of the ^{7}Be core. Moreover, we assume that the spectroscopic factor for this configuration is equal to one.

2.2. Single-particle Hamiltonian

We adopt the single-particle model suggested by Robertson [5] for a proton interacting with the ^{7}Be core. The core is assumed to be inert, with an intrinsic spin $I_A = 3/2^-$. The proton wave function, labelled by angular momentum (ℓj), is coupled to the core spin to form the total channel spin J. The interaction between the proton and the core is parametrized as a Coulomb interaction and a Woods–Saxon plus spin–orbit nuclear potential, with an adjustable depth $V_0(\ell(jI_A)J)$ for each channel,

$$V(r) = V_0(\ell(jI_A)J)\left(1 - F_{\text{s.o.}}(\boldsymbol{l}\cdot\boldsymbol{s})\frac{r_0}{r}\frac{d}{dr}\right)f(r), \tag{2.1}$$

where

$$f(r) = \left(1 + \exp[(r-R)/a)]\right)^{-1}. \tag{2.1'}$$

Adjusting the depth allows us to reproduce the energy of known states. We use $a = 0.52$ fm and $r_0 = 1.25$ fm, and discuss our choice for the radius, $R = 2.391$ fm, in Subsection 3.2. The spin–orbit strength is set to $F_{\text{s.o.}} = 0.351$ fm. This is consistent with Robertson's choice but slightly smaller than the value 0.38 fm which is realistic for the low-lying spectra of ^{17}O, ^{13}C and ^{11}Be, cf. Ref. [6].

The well depth for the ground state channel, $\ell(jI_A)J = (p_{3/2}, 3/2^-)2^+$, was adjusted to reproduce the one-proton separation energy and is $V_0((p_{3/2}, 3/2^-)2^+) = -44.658$ MeV. Similarly, the observed $J = 1^+$ and 3^+ resonances in ^{8}B are described as $p_{3/2}$ waves coupled to the ground state of the core, and the well depths for these channels, -42.14 and -36.80 MeV respectively, have been adjusted to reproduce the known resonance energies [7]. A $p_{3/2}$ wave and the spin of the core can also couple to the total spin $J = 0^+$ but we shall completely ignore this channel since it appears to be very weak in the low-lying excitation spectrum of ^{8}B; it would increase the quadrupole response discussed in Subsection 3.1 by less than 5%. For all other partial waves ($s_{1/2}$, $p_{1/2}$, $d_{3/2}$, etc.) we choose identical well depths and set them equal to the value -42.14 MeV we obtained for the $(p_{3/2}, 3/2^-)1^+$ channel, as suggested by Robertson [5].

2.3. Wave functions and matrix elements

The channel wave functions have the form

$$\Psi_{JM} = \frac{\phi^J_{k\ell j}(r)}{r}\sum_{mM_A}\langle jmI_AM_A|JM\rangle|jm\rangle|I_AM_A\rangle. \tag{2.2}$$

Here $\phi^J_{k\ell j}$ is the radial wave function for the relative motion of the proton and the core, normalized to $\sqrt{2/\pi}\sin(kr+\delta^J_{\ell j})$ at large r. The ground state wave function has a form similar to Eq. (2.2); we denote it by $|\ell_0(j_0I_A))J_0\rangle$.

The Coulomb field from a target nucleus acts on both the proton and the core. We are here concerned with the component that excites the relative motion of the proton,

$(Z_x, A_x) = (1,1)$, and the core, $(Z_c, A_c) = (4,7)$, and express it in terms of the electric multipole operators, $\mathcal{M}_{\lambda\mu} = e_\lambda r^\lambda Y_{\lambda\mu}(\hat{r})$, with the effective multipole charge

$$e_\lambda = Z_c e\left(\frac{-A_x}{A_x + A_c}\right)^\lambda + Z_x e\left(1 - \frac{A_x}{A_x + A_c}\right)^\lambda. \tag{2.3}$$

It is convenient to express matrix elements of the multipole operators in terms of reduced matrix elements, and we shall use the convention of Ref. [8], Eq. (1A-60),

$$\langle JM|\mathcal{M}_{\lambda\mu}|J_0M_0\rangle = \langle J_0M_0\lambda\mu|JM\rangle \frac{\langle J\|\mathcal{M}_\lambda\|J_0\rangle}{\sqrt{2J+1}}, \tag{2.4}$$

where $\langle J_0M_0\lambda\mu|JM\rangle$ is the Clebsch–Gordan coefficient. From the single-particle wave functions, we can calculate the reduced single-particle matrix elements, $\langle k\ell j\|\mathcal{M}_\lambda\|\ell_0 j_0\rangle_J$. Here the subscript J is a reminder that the matrix element depends on the channel spin J, because we have used different single-particle Hamiltonians in the different channels. The reduced matrix element in Eq. (2.4) can be obtained from a standard formula of angular momentum algebra, e.g. Eq. (7.17) of Ref. [9]. The result is

$$\langle J\|\mathcal{M}_\lambda\|J_0\rangle = (-1)^{j+I_A+J_0+\lambda}[(2J+1)(2J_0+1)]^{1/2} \times \begin{Bmatrix} jJI_A \\ J_0 j_0 \lambda \end{Bmatrix} \langle k\ell j\|\mathcal{M}_\lambda\|\ell_0 j_0\rangle_J. \tag{2.5}$$

The multipole strength in a particular partial wave, $(k\ell j)$, summed over all final channel spins is

$$\frac{dB(\mathrm{E}\lambda;\ell_0 j_0 \to k\ell j)}{dk} = \sum_J \frac{|\langle J\|\mathcal{M}_\lambda\|J_0\rangle|^2}{2J_0+1} = \sum_J (2J+1)\begin{Bmatrix} jJI_A \\ J_0 j_0 \lambda \end{Bmatrix}^2 |\langle j\|\mathcal{M}_\lambda\|j_0\rangle|^2_J. \tag{2.6}$$

It reduces to the usual single-particle strength, $|\langle j\|\mathcal{M}_\lambda\|j_0\rangle|^2/(2j_0+1)$, if the single-particle matrix elements are independent of the channel spin J. This follows directly from a basic sum rule for the $6j$ symbols.

The total multipole strength is obtained by summing over all partial waves,

$$\frac{dB(\mathrm{E}\lambda)}{dk} = \sum_{\ell j} \frac{dB(\mathrm{E}\lambda;\ell_0 j_0 \to k\ell j)}{dk}. \tag{2.7}$$

It is here expressed as a differential in k. This is the result one obtains when the continuum wave functions are normalized as mentioned below Eq. (2.2). We shall often make use of the total strength as a differential in the kinetic energy for the relative motion of the two fragments. This is given by

$$\frac{dB(\mathrm{E}\lambda)}{dE} = \mu_{xc}\frac{dB(\mathrm{E}\lambda)}{kdk}, \tag{2.8}$$

where μ_{xc} is the reduced mass for the two fragments.

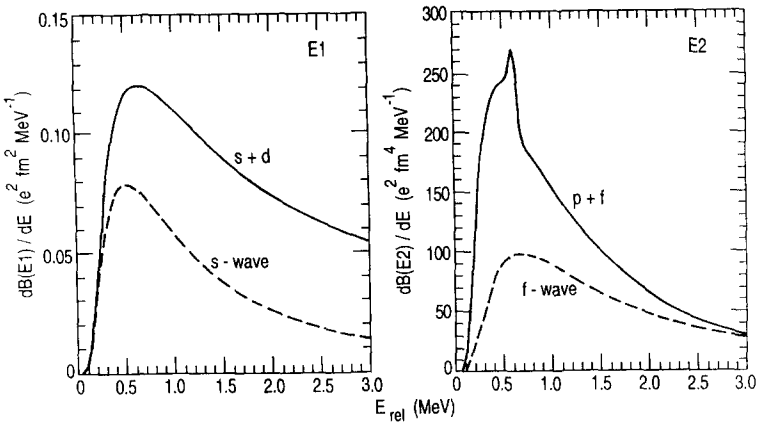

Fig. 1. Calculated dipole (E1) and quadrupole (E2) responses of ^{8}B, as functions of the relative kinetic energy in the final state. The dashed curves are the separate contributions from the final state s- and f-waves.

3. Radiative capture and Coulomb dissociation

Here we present some of the basic results that our model predicts for ^{8}B, namely the electric dipole (E1) and quadrupole (E2) responses, the associated S-factors for the radiative capture of protons on ^{7}Be, and finally, the decay energy spectrum for the ^{8}B $\rightarrow$ ^{7}Be+p Coulomb dissociation on a lead target.

A critical issue which has been debated in the literature [2,10,11] is the importance of E2 transitions in the Coulomb dissociation experiment [1]. The point is that if the dissociation is completely dominated by E1 transitions, then one can fairly accurately extract the dipole response and next infer the radiative E1 capture rate. However, if E2 transitions make a significant contribution, this procedure would become much more uncertain and one would have to rely on a model for the E2 component, as was done in Ref. [2]. Our model, presented in Section 2, makes certain predictions which may or may not be realistic. We comment on that below as we present our results and make comparisons to other model predictions and to measurements.

3.1. Electric multipole responses

The electric dipole and quadrupole strength functions that we have calculated for the ^{8}B $\rightarrow$ ^{7}Be+p breakup are shown in Fig. 1 as functions of the final state kinetic energy for the relative motion of the two fragments. For the dipole strength function we also show the contribution from final state s-waves (dashed curve). They clearly dominate at low excitation energies but d-waves become quite important at 0.6 MeV (30% of the total) and they start to dominate at even higher excitation energies.

The quadrupole strength has a peak at about 0.6 MeV, which reflects the resonance in the $p_{3/2}$ continuum associated with the 1^+ channel. Also shown in Fig. 1 is the contribution from final state f-waves ($f_{5/2}$ and $f_{7/2}$). They are seen to be quite important

at 0.6 MeV and at higher excitation energies, and it is not justified to neglect them.

3.2. Radiative capture

The cross section for the radiative capture, $a + b \rightarrow c + \gamma$, is related to the photoabsorption cross section for the inverse reaction, $c + \gamma \rightarrow a + b$, by detailed balance [12]. For a given electric multipole transition the relation is

$$\sigma_{\mathrm{E}\lambda}^{(rc)} = \left(\frac{E_\gamma}{\hbar c k}\right)^2 \frac{2(2I_c+1)}{(2I_a+1)(2I_b+1)} \sigma_{\mathrm{E}\lambda}^{(\gamma)} . \tag{3.1}$$

Here E_γ is the photon energy, and $\hbar k$ is the momentum for the relative motion of a and b. The expression contains the ratio of the phase space factors for the photon and for the relative motion of a and b, and the statistical weights associated with the spins in the initial and final states. In the case of ^{8}B we have $I_c = 2$, and $I_a = 3/2$ and $I_b = 1/2$ are the ground state spins of ^{7}Be and the proton. The additional factor of two in (3.1) accounts for the two possible polarizations of the photons emitted in the radiative capture process.

The photoabsorption cross section, on the other hand, can be expressed in terms of the multipole response, Eq. (2.8), as follows (cf. Eq. 3C-16 of Ref. [8]):

$$\sigma_{\mathrm{E}\lambda}^{(\gamma)} = \frac{(2\pi)^3(\lambda+1)}{\lambda((2\lambda+1)!!)^2} \left(\frac{E_\gamma}{\hbar c}\right)^{2\lambda-1} \frac{dB(\mathrm{E}\lambda)}{dE_\gamma} . \tag{3.2}$$

The cross section for the radiative capture of charged particles is usually expressed in terms of the S-factor,

$$S(E_{\mathrm{rel}}) = E_{\mathrm{rel}} \sigma_{\mathrm{E}\lambda}^{(rc)} \exp[2\pi\eta(E_{\mathrm{rel}})] , \tag{3.3}$$

where $E_{\mathrm{rel}} = \frac{1}{2}\mu_{ab} v_{\mathrm{rel}}^2$ is the relative kinetic energy of the two particles and $\eta = Z_a Z_b e^2/(\hbar v_{\mathrm{rel}})$. Inserting (3.1) and (3.2) into this expression, one can now calculate the S-factor directly from the multipole response. The results we obtain are shown in Fig. 2. Note that the E2 result has been multiplied by a factor of 100, so E2 transitions play an insignificant role in the radiative capture.

The total S-factor we obtain at low energies (around 100 keV) is of the order of 17 eV b. This is at the lower end of most radiative capture measurements but not far from the most recent one of Filippone et al. [13], and it is in fair agreement with the value inferred from the recent Coulomb dissociation measurement [1]. In fact, we have chosen the radius of the ^{7}Be core, $R = 2.391$ fm, so that the S-factor would fall in this range. If we choose a larger radius (say 2.95 fm) we obtain a larger S-factor, which is close to the values obtained in Refs. [14,15]. The E2 contribution is smaller than the value obtained by Kim et al. [14] (by 25% at 0.5 MeV), but it is about twice the value obtained by Typel and Baur [15], mainly because they neglected the final state f-waves which play a significant role, cf. Fig. 1.

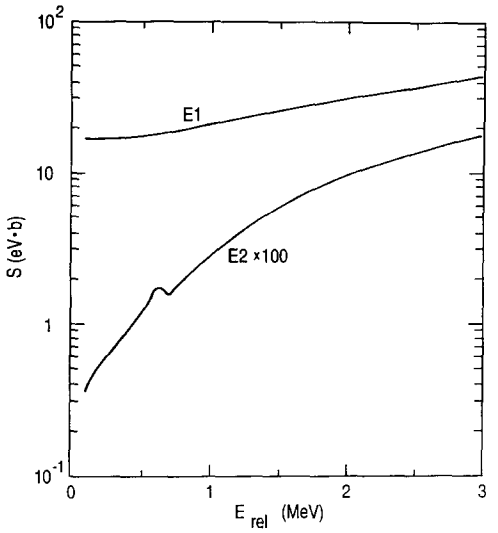

Fig. 2. Calculated S-factors for the radiative capture of protons on ^{7}Be. Results for E1 and E2 transitions are shown as functions of the relative kinetic energy. Note that the S-factor for E2 transitions has been multiplied by 100.

3.3. Coulomb dissociation

For the present we treat the Coulomb excitation of ^{8}B in first-order perturbation theory. The dissociation probability is calculated from the electric multipole strength functions with the formulas of Ref. [16]. These formulas assume a straight-line trajectory for the projectile as well as first-order perturbation theory. The amplitude for the electric Coulomb excitation to a particular final state, $|k\ell(jI_A)JM\rangle$, can be written as

$$a_{fi} = -i\sum_{\lambda\mu} F_{\lambda\mu}\langle k\ell(jI_A)JM|\mathcal{M}_{\lambda\mu}|\ell_0(j_0I_A)J_0M_0\rangle. \tag{3.4}$$

The F-amplitudes are here given by

$$F_{\lambda\mu} = i^{\lambda+\mu}\,\frac{Z_1 e}{\hbar v\gamma}\sqrt{\frac{16\pi}{2\lambda+1}}\,\frac{(\omega/v)^\lambda \widetilde{G}_{\lambda\mu}}{\sqrt{(\lambda+\mu)!(\lambda-\mu)!}}\,K_\mu(\xi), \tag{3.5}$$

where Z_1 is the charge number of the projectile. These amplitudes depend on the excitation energy $\hbar\omega$, the beam velocity v, and $\gamma = 1/\sqrt{1-(v/c)^2}$. They also depend on the impact parameter b through the argument of the modified Bessel function $K_\mu(\xi)$, $\xi = \omega b/(\gamma v)$. In our numerical applications we shall use the improved expression for ξ, Eq. (2.24) of Ref. [16], which includes a correction due to the fact that the trajectory is not a straight line.

The $\widetilde{G}_{\lambda\mu}$ in Eq. (3.5) is equal to one in the non-relativistic limit. We use the relativistic expressions

$$\widetilde{G}_{10} = \widetilde{G}_{20} = \widetilde{G}_{2\pm2} = \frac{1}{\gamma}, \qquad \widetilde{G}_{1\pm1} = 1, \qquad \widetilde{G}_{2\pm1} = \frac{1}{2}\left(1+\frac{1}{\gamma^2}\right), \tag{3.6}$$

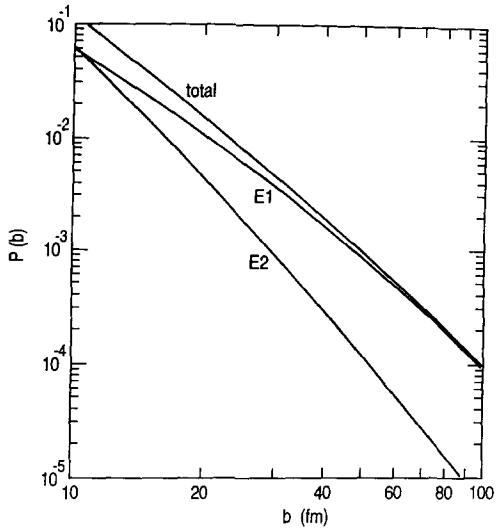

Fig. 3. Calculated Coulomb dissociation probabilities for ^{8}B, as functions of impact parameter with respect to a lead nucleus, at a beam energy of 46.5 MeV/u. The three curves show, in increasing order, the separate results of E2 and E1 transitions, and the sum.

which can be derived from Ref. [16]. The amplitude for magnetic excitations are also given in Ref. [16] but we shall not consider them here.

The phases of the amplitudes (3.4), (3.5) assume that the projectile moves in the positive z-direction and the x-axis is in the scattering plane, pointing towards the projectile trajectory [16]. For our purposes in this section we only need the angle-integrated excitation probability, which is given by

$$\frac{dP(E,b)}{dE} = \sum_{\lambda\mu} |F_{\lambda\mu}|^2 \, \frac{1}{2\lambda+1} \, \frac{dB(\mathrm{E}\lambda)}{dE}. \tag{3.7}$$

In our numerical example, we choose a beam energy of 46.5 MeV/u and use the Coulomb field from a lead nucleus to generate the excitation of ^{8}B, as was done in a recent experiment [1]. The E1 and E2 dissociation probabilities (integrated over all excitation energies) and their sum are shown in Fig. 3 as functions of the impact parameter. The E2 probability is seen to fall off much faster than the E1 probability. In Fig. 4 we show the decay energy spectrum, i.e. the dissociation cross section as a differential in the relative kinetic energy. We show the E2 contribution (dashed curve), the E1 contribution (dotted curve), and the sum (solid curve), together with the data [1] which have here been divided by the detection efficiency. The minimum impact parameter was chosen to be 20 fm so that the magnitude of the calculated cross section is close to the measurement.

We emphasize that the comparison to the data may not be completely realistic since we have used a sharp cutoff in the impact parameter, whereas the measurement has a diffuse detection efficiency as function of impact parameter. The 20 fm cutoff corresponds to a ^{8}B scattering angle of 4.5°, which is larger than the range of angles where the detector

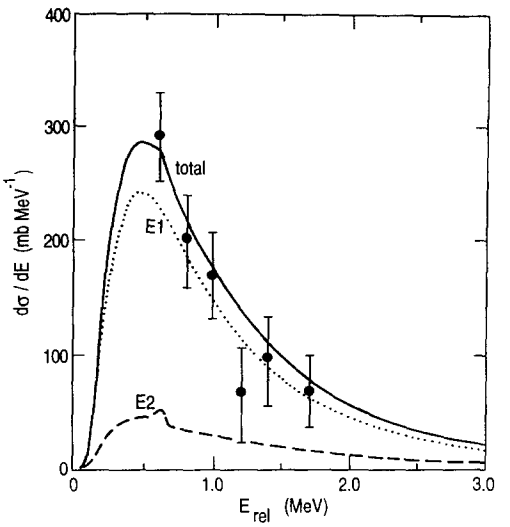

Fig. 4. Coulomb dissociation cross section for ^{8}B as a function of the relative kinetic energy in the ^{7}Be+p final state, for a beam energy of 46.5 MeV/u on a lead target. The three curves show the E1 (dotted) and E2 (dashed curve) contributions, and the sum (solid curve). The minimum impact parameter was set to 20 fm. Also shown are the data from Ref. [1].

efficiency is flat. Our results indicate that the E2 contribution is present in the experiment but it is of the order of or smaller than the experimental resolution. We shall see in Section 6 that higher-order dynamical processes effectively reduce the influence of E2 transitions at the peak.

4. Angular and momentum distributions

Independent information about the significance of E2 transitions in the target may be obtained from the angular distribution of the proton and the residual ^{7}Be. The same purpose may be achieved by measuring the distribution in momentum instead of angle. Such distributions can be derived from the Coulomb excitation amplitudes (3.4), (3.5). We remind the reader of the coordinate definitions in these formulas. The reference frame has its origin at the target nucleus, which in the present context is ^{8}B. The z-axis points in the direction of the projectile velocity. The x-axis is in the scattering plane, pointing towards the projectile trajectory, which has the coordinates $(x, y, z) = (b, 0, vt)$. We shall keep this convention in this section. In Section 5 we apply the expressions we derive to radioactive beam experiments, where the role of projectile and target is interchanged.

The momentum space wave function for the relative motion of the two fragments, obtained from the amplitudes (3.4), is given by the sum over all final states,

$$\Psi^{(f)}(\boldsymbol{k}, b) = \frac{1}{k} \sum_{\ell j m J M} a_{fi} \exp(i\delta^J_{\ell j}(k)) \langle j m I_A M_A | J M \rangle \langle \hat{\boldsymbol{k}} | \ell j m \rangle, \tag{4.1}$$

for a given initial state and a given impact parameter b. Note that the spin of the core, (I_A, M_A), is the same in the initial and final state in our single-particle model. The sum (4.1) includes the partial wave phase shifts, $\delta_{\ell j}^{(J)}(k) = \delta_C + \delta_N - \ell\pi/2$, due to the Coulomb, nuclear and centrifugal potentials of the single-particle Hamiltonian. From this expression one can now directly calculate the final state momentum distribution. However, this approach is only convenient, from a numerical point of view, in simple cases. An example is discussed in Appendix A. In general, it is more economical to express the angular distribution as a multipole expansion and calculate the multipole coefficients separately.

4.1. Angular distribution

The formula for the angular distribution involves interference between E1 and E2 amplitudes. It is convenient to express the Coulomb excitation probability with the angular-momentum coupled product of $F_{\lambda\mu}$ and its complex conjugate. Specifically, we define the quantity

$$f(\lambda_1, \lambda_2; \Lambda M) = \sum_{\mu\mu'} F_{\lambda\mu} F^*_{\lambda'\mu'} \langle \lambda\mu\Lambda M | \lambda'\mu' \rangle. \tag{4.2}$$

This will lead to an angular distribution proportional to the Wigner $\mathcal{D}$-function, $\mathcal{D}^{\Lambda}_{M0}$. The formula has the form

$$\frac{dP(k,b)}{dk\, d\Omega} = \frac{1}{4\pi} \sum_{\lambda_1\lambda_2} {\sum_{\Lambda M}}' f(\lambda_1\lambda_2; \Lambda M) \left(\mathcal{D}^{\Lambda}_{M0}(\hat{k})\right)^* A^{\Lambda}_{\lambda_1\lambda_2}, \tag{4.3a}$$

where the sum with the prime is restricted to Λ-values such that $\lambda_1 + \Lambda - \lambda_2$ is even. Note that Eq. (4.2) implies a selection rule for allowed Λ, $|\lambda_1 - \lambda_2| \leqslant \Lambda \leqslant \lambda_1 + \lambda_2$. The coefficient $A^{\Lambda}_{\lambda_1\lambda_2}$ is given by the product of reduced matrix elements, phase shifts factors, and angular recoupling coefficients as

$$A^{\Lambda}_{\lambda_1\lambda_2} = \sum_{\ell_1 j_1 J_1} \sum_{\ell_2 j_2 J_2} \langle J_1 \| \mathcal{M}_{\lambda_1} \| J_0 \rangle \langle J_2 \| \mathcal{M}_{\lambda_2} \| J_0 \rangle^* e^{i(\delta^{J_1}_{\ell_1 j_1} - \delta^{J_2}_{\ell_2 j_2})} C^{\Lambda}_{1,2}. \tag{4.3b}$$

The coefficient $C^{\Lambda}_{1,2}$ in the above equation may be expressed with Clebsch–Gordan coefficients as

$$\begin{aligned} C^{\Lambda}_{1,2} = {} & \frac{(-1)^{\Lambda + j_1 + j_2 - 1}}{2J_0 + 1} \frac{(2\Lambda+1)^2}{(2j_2+1)(2\lambda_2+1)} \sqrt{\frac{(2j_1+1)(2j_2+1)}{(2J_1+1)(2J_2+1)}} \langle j_1 \tfrac{1}{2} \Lambda 0 | j_2 \tfrac{1}{2} \rangle \\ & \times \sum_{\mu m M M_0 M_A} \langle \lambda_1 \mu \Lambda 0 | \lambda_2 \mu \rangle \langle J_0 M_0 \lambda_1 \mu | J_1 M \rangle \langle j_1 m I_A M_A | J_1 M \rangle \\ & \times \langle J_0 M_0 \lambda_2 \mu | J_2 M \rangle \langle j_2 m I_A M_A | J_2 M \rangle \langle j_1 m \Lambda 0 | j_2 m \rangle. \end{aligned} \tag{4.3c}$$

The expressions (4.3a)–(4.3c) are consistent with the result obtained in Ref. [17] if one considers the simpler case of $I_A = 0$, with a single electric multipole excitation, and performs an angular average around the beam direction.

The sum over the six Clebsch-Gordan coefficients in Eq. (4.3c) can be reduced to a factor times two $6j$-symbols [18]. This permits the following equivalent expression for the C-coefficient:

$$C^{\Lambda}_{1,2} = (-1)^{J_0+J_1-J_2-I_a-j_1-\lambda_1-1}\frac{2\Lambda+1}{2J_0+1} \times \left(\frac{(2J_1+1)(2J_2+1)(2j_1+1)}{2\lambda_2+1}\right)^{1/2} \langle j_1 \tfrac{1}{2} \Lambda 0 | j_2 \tfrac{1}{2}\rangle \begin{Bmatrix} J_2 \lambda_2 J_0 \\ \lambda_1 J_1 \Lambda \end{Bmatrix} \begin{Bmatrix} J_2 j_2 J_0 \\ j_1 J_1 \Lambda \end{Bmatrix}. \tag{4.3d}$$

There are restrictions on the multipolarities in the angular distribution when only electric transitions are present. Thus the angular distribution (4.3) obeys the selection rule that $\lambda_1 + \Lambda - \lambda_2$ is even. This is indicated by the prime on the sum in Eqs. (4.3a) and (4.7) and follows from the fact that $\ell_i + \lambda - \ell_0$ $(i = 1, 2)$ is even for electric transitions, and Λ is basically obtained by coupling ℓ_1 and ℓ_2 for even values of $\ell_1 + \Lambda - \ell_2$.

We note that the functions defined in Eq. (4.3b) fulfill the relation

$$A^{\Lambda}_{\lambda_1\lambda_2}(k) = (-1)^{\lambda_1-\lambda_2}\sqrt{\frac{2\lambda_1+1}{2\lambda_2+1}}\left(A^{\Lambda}_{\lambda_2,\lambda_1}(k)\right)^{*}. \tag{4.4}$$

This implies that the functions $A^{\Lambda}_{\lambda\lambda}(k)$ are real. These functions are particularly simple for $\Lambda = 0$,

$$A^{0}_{\lambda\lambda}(k) = \frac{1}{(2\lambda+1)(2J_0+1)}\sum_{\ell j J}|\langle k\ell(jI_A)J\|\mathcal{M}_{\lambda}\|\ell_0(j_0 I_A)J_0\rangle|^2, \tag{4.5}$$

which is just the multipole response, Eq. (2.7), divided by $2\lambda + 1$; they obviously generate the spherical part of the angular distribution.

Finally we note that the angular distribution is symmetric under reflections in the scattering plane, i.e. for $y \to -y$ or $\phi \to -\phi$, simply because the exciting Coulomb interaction has this symmetry. This implies that only the real part of the $\mathcal{D}$-functions is effective in the sum (4.3a). Moreover, it is useful to extract the phase factors of the F-amplitudes,

$$F_{\lambda_1\mu_1}F_{\lambda_2\mu_2} = i^{\lambda_1-\lambda_2-M}\,|F_{\lambda_1\mu_1}F_{\lambda_2\mu_2}|, \tag{4.6}$$

where $M = \mu_2 - \mu_1$, and the absolute value of the F-factors is independent of the signs of the μ's, cf. Eq. (3.5). We can now write the angular distribution as

$$\frac{dP(k,b)}{dk\,d\Omega} = \frac{1}{4\pi}\sum_{\lambda_1\mu_1\lambda_2\mu_2}|F_{\lambda_1\mu_1}F_{\lambda_2\mu_2}|\sum_{\Lambda,M}{}'\langle\lambda_1\mu_1\Lambda M|\lambda_2\mu_2\rangle \times \mathrm{Re}\left(i^{\lambda_1-\lambda_2-M}A^{\Lambda}_{\lambda_1\lambda_2}(k)\right)\mathrm{Re}\left(\mathcal{D}^{\Lambda}_{M0}(\hat{k})\right), \tag{4.7}$$

where the prime has the same meaning as in Eq. (4.3a). This result shows, in particular, that M must be even if $\lambda_1 = \lambda_2$ since the A-functions are real in this case according to Eq. (4.4).

4.2. Longitudinal momentum distribution

A commonly measured observable in breakup reactions is the longitudinal momentum distribution. It can be obtained from Eq. (4.7) by integrating over all transverse momenta for fixed k_z,

$$\frac{dP(k_z,b)}{dk_z} = \int_0^\infty k_\perp dk_\perp \frac{1}{k^2} \int_0^{2\pi} d\phi \frac{dP(\boldsymbol{k},b)}{dk\, d\Omega}. \tag{4.8}$$

The ϕ-integration implies that only terms with $M = 0$ will survive in Eq. (4.7). Thus we obtain

$$\frac{dP(k_z,b)}{dk_z} = \frac{1}{2} \sum_{\Lambda\lambda_1\lambda_2\mu} \langle \lambda_1 \mu \Lambda 0 | \lambda_2 \mu \rangle \int_{|k_z|}^\infty \frac{dk}{k} |F_{\lambda_1\mu} F_{\lambda_2\mu}|\, i^{\lambda_1-\lambda_2}\, A^\Lambda_{\lambda_1\lambda_2}(k)\, P_\Lambda(\frac{k_z}{k}). \tag{4.9}$$

The differential cross section can now be obtained by integrating over all impact parameters larger than a certain cutoff $b_{\min}$, which is determined by the experimental acceptance. This integration can be performed analytically [16].

5. Calculated distributions

The expression for the angular distribution of protons, Eq. (4.7), was derived for Coulomb dissociation of a target nucleus. In this section we consider the dissociation of the projectile in a radioactive beam experiment. Thus we choose the beam direction as the z-axis but keep the x-axis in the reaction plane, pointing towards the target nucleus. The two reference frames are connected by the transformation, $(x, y, z) \rightarrow (x, -y, -z)$. Since Eq. (4.7) is symmetric with respect to reflections in the reaction plane (i.e. $y \rightarrow -y$), we can obtain the new distribution simply by changing the direction of the z-axis.

Here we present the calculated angular and momentum distributions of protons emitted in Coulomb dissociation of ^{8}B. The distributions are presented as differential cross sections and they all refer to the rest frame of the ^{7}Be+p system. We choose a ^{8}B beam energy of 46.5 MeV/u on a lead target and a minimum impact parameter of 20 fm, as we did in Subsection 3.3. We also show two examples on the longitudinal momentum distribution of ^{7}Be fragments and compare the width to a recent measurement. This distribution is obtained from the proton distribution by making use of momentum conservation in the rest frame of the ^{7}Be+proton system.

5.1. Angular distributions

Angular distributions are shown in Fig. 5 for a final state kinetic energy of 0.6 MeV. They are shown as differentials in $\cos\theta$, where θ is the angle with respect to the

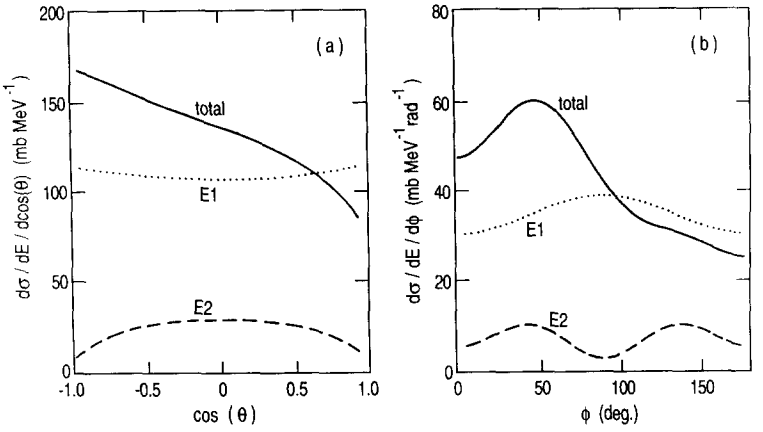

Fig. 5. Angular distributions of protons emitted in the Coulomb dissociation of ^{8}B on a lead target at 46.5 MeV/u. They are shown in (a) and (b) as differential cross sections in $\cos\theta$ and in the azimuthal angle ϕ, respectively, for a final state kinetic energy of 0.6 MeV. The dotted and dashed curves are the separate results for E1 and E2 transitions, and the solid curves are the full result of the E1+E2 interference.

radioactive beam axis, and in ϕ which is the azimuthal angle with respect to the reaction plane. The latter distribution is only shown for $0 \leqslant \phi \leqslant 180°$, since it is symmetric with respect to reflections in the reaction plane. The dotted and dashed curves are the separate distributions generated by pure E1 and E2 transitions, respectively. The solid curves show the combined result. Clearly, the interference between E1 and E2 transitions has a dramatic effect and produces large asymmetries.

The interference pattern is rather insensitive to the final state kinetic energy. It depends on the impact parameter, and the largest asymmetries appear at smaller impact parameters, where the relative magnitude of E2 transitions is larger, cf. Fig. 3. This trend can be seen by comparing Fig. 5 to Fig. 2 of Ref. [3], which was obtained at a fixed impact parameter of 20 fm but otherwise under the same conditions as Fig. 5.

The qualitative behavior of the asymmetries in $\cos\theta$ and ϕ can be understood from physical arguments. The time-dependent Coulomb field from the target nucleus accelerates the proton in the direction of motion of that field, producing an enhancement at negative values of $\cos\theta$. The ϕ-distribution shows an enhanced emission of protons in the direction of the exciting Coulomb field, i.e. favoring $\phi = 0$ over $\phi = \pi$. This behavior can be understood as follows. The Coulomb (dipole plus quadrupole) field is stronger when the proton is on the same side of the ^{8}B nucleus as the exciting field, and most of the protons are therefore emitted from that side. These protons are then accelerated in the Coulomb field from the ^{7}Be core and they acquire a velocity in the direction towards the exciting field. This mechanism depends on the Coulomb field from the ^{7}Be and gives no asymmetry in the absence of final state interactions between the ^{7}Be and the proton.

The qualitative features of the interference pattern may be seen in more detail from a simple example worked out in Appendix A. There it is assumed that the valence nucleon is initially bound in an s-wave, and the Coulomb and nuclear interactions with the core

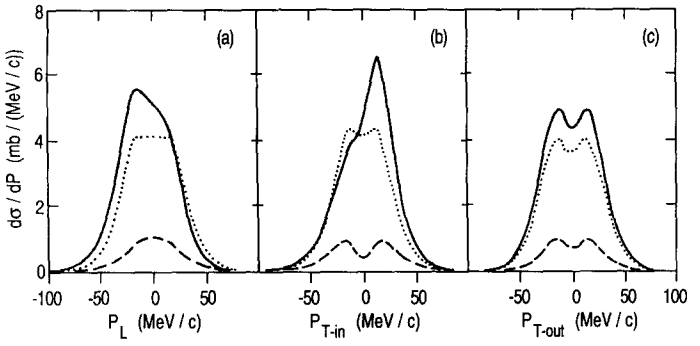

Fig. 6. Momentum distributions of protons emitted in the Coulomb dissociation of ^{8}B on a lead target at 46.5 MeV/u. Three projections are shown, namely the longitudinal (a), the transverse in-plane (b), and the transverse out-of-plane distribution (c). In each case we show the result of pure E1 (dotted) and E2 transitions (dashed), and the full result of the E1+E2 interference (solid curve).

are set to zero in the final state. The analytic expression one then obtains, Eq. (A.5), clearly exhibits the interference pattern that is seen in the $\cos\theta$ distribution of Fig. 5. The ϕ-distribution that one obtains from Eq. (A.5) turns out to be symmetric around 90°. This result is consistent with the explanation given above that it is the final state interaction of the proton with the core, in particular the repulsive Coulomb field, that is responsible for the observed asymmetry in the ϕ-distribution.

Let us finally point out that the angular distributions obtained for pure E1 dissociation, shown by the dotted curves in Fig. 5, are almost isotropic. Moreover, they are very different from the angular distributions of neutrons measured by Nakamura et al. [19] in the ^{11}Be→^{10}Be+n breakup reaction. The main reason is that the valence proton in ^{8}B is bound in a p-wave, whereas the valence neutron in ^{11}Be is bound in an s-wave. This qualitative difference is discussed in detail in Appendix B. We also note that the angular distribution of neutrons is insensitive to the E1+E2 interference because the effective quadrupole charge (2.3) is quite small for a neutron halo.

5.2. *Momentum distributions*

The angular distributions of protons can also be converted into a momentum distribution and we show the three projections in Fig. 6, namely the longitudinal (along the beam axis), the transverse in-plane (i.e. in the reaction plane) and finally the transverse out-of-plane distribution. The dotted and dashed curves are the results of pure E1 and E2 dissociation, respectively, and the solid curves are the combined result of the E1 and E2 interference.

The longitudinal and the transverse in-plane distributions are both asymmetric in a way that is consistent with the angular distributions shown in Fig. 5. The maxima are located at -15 MeV/c and $+15$ MeV/c, respectively, which amounts to 5% of the beam momentum per particle. The transverse out-of-plane distribution is symmetric because of the reflection symmetry with respect to the reaction plane discussed earlier.

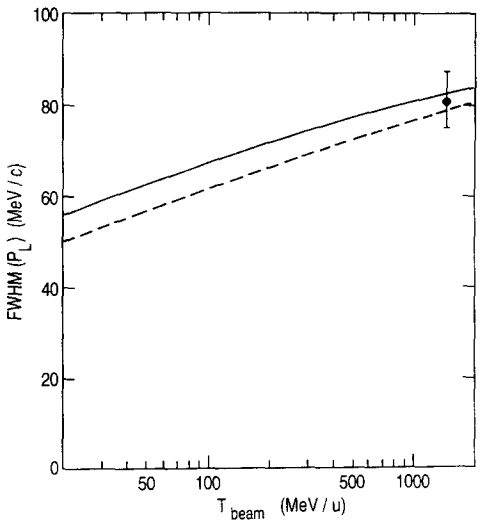

Fig. 7. Beam energy dependence of the width (FWHM) of the longitudinal momentum distribution of ^{7}Be fragments, emitted in the Coulomb dissociation of ^{8}B on a lead target. The minimum impact parameter was set to 20 fm (solid curve) and 40 fm (dashed curve), respectively. The data point is from Ref. [21].

We note that the three distributions shown by the dotted curves in Fig. 6, obtained for pure E1 dissociation, are not much different. This is a consequence of the nearly isotropic angular distribution one obtains for E1 transitions when the initial state of the proton is a p-wave. In contrast, the three distributions are quite different from those one obtains for neutrons that are bound in an s-wave. An example is illustrated in Fig. 4 of Ref. [20] where the dashed curves show the same set of distributions for the di-neutron initially bound in an s-wave and emitted in the E1 Coulomb dissociation of ^{11}Li.

5.3. Comparison to measurements

All three projections of the momentum distribution discussed above have not yet been measured. Only the longitudinal momentum distribution of ^{7}Be fragments has been measured at 1471 MeV/u on a lead target [21], and more recently at 40 MeV/u on a gold target [22]. However, only the width (FWHM) obtained in the high-energy experiment has been published and it is shown in Fig. 7 together with our predictions for two different choices on the minimum impact parameter, namely 20 fm (solid curve) and 40 fm (dashed curve). The most realistic value depends of the angular acceptance of the measurement. Anyway, both predictions are consistent with the measurement.

We note that the calculated width increases with increasing beam energy. This shows that the width is sensitive to the reaction mechanism, which in this context is Coulomb dissociation. The width obtained in nuclear induced breakup reactions (i.e. on a light target) is expected to have a much weaker dependence on the beam energy. The fact

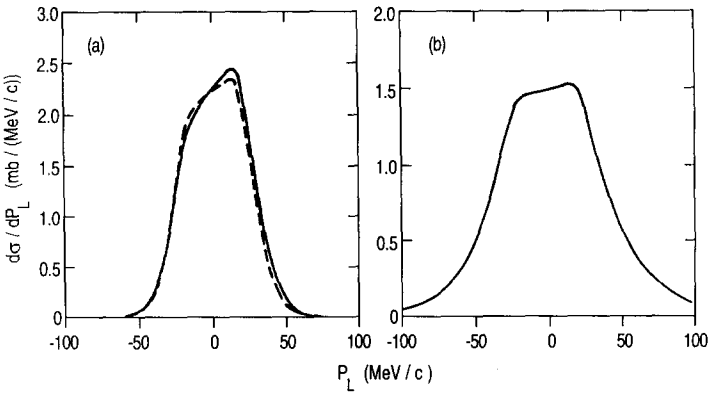

Fig. 8. Longitudinal momentum distributions of ^{7}Be fragments emitted in the Coulomb dissociation of ^{8}B on a gold target at 40 MeV/u (a) and on a lead target at 1471 MeV/u (b), for a minimum impact parameter of 40 and 20 fm, respectively. The solid curves are the result of the E1+E2 interference in first order perturbation theory. The dashed curve in (a) is the result of the dynamical calculations discussed in Section 6.

that the measured widths in the high-energy experiment [21] are identical for light and heavy targets is probably accidental. Thus repeating the measurement at a much lower beam energy we expect that the width will be decreasing with increasing atomic number of the target.

We have also studied the sensitivity to the choice of the radius parameter in the proton-core Hamiltonian, Eq. (2.1′). Thus by increasing the radius from 2.391 fm to 2.95 fm, and re-adjusting the well depths so that we reproduce the binding and the two known resonances in ^{8}B as we did in Subsection 2.2, we find that the r.m.s. proton-core distance increases from 4.24 to 4.64 fm. This leads to larger multipole strengths and larger Coulomb dissociation cross sections but the width of the longitudinal momentum distribution does not change significantly.

The longitudinal momentum distributions of ^{7}Be fragments that we obtain on a gold target at 40 MeV/u and on a lead target at 1471 MeV/u are shown by the solid curves in Figs. 8a and b, respectively.

The minimum impact parameter was set to 40 fm at the lower beam energy and 20 fm at the higher beam energy. The distribution at the higher beam energy is much broader (cf. Fig. 7) and the tails are much larger than at the lower beam energy. The asymmetry, however, is much larger at the smaller beam energy simply because the E2 component is relatively more important in this case, even though we have chosen a larger, minimum impact parameter.

By measuring the asymmetry of the longitudinal momentum distribution one should be able to get a handle on the magnitude of the E2 strength. However, before one can extract this strength from measurements it is important first to understand the influence of higher-order dynamical processes. This is discussed in detail in the next section. We find that higher-order processes reduce the asymmetry. This is illustrated by the dashed curve in Fig. 8a.

6. Higher-order dynamical effects

A critical issue is the influence of higher-order processes in the Coulomb field from the target nucleus. We have therefore also performed dynamical calculations of the Coulomb dissociation which are similar to those presented in Ref. [20]. In order to simplify the calculation we set the spin of the core to zero and ignore the spin–orbit interaction in the single-particle potential (2.1), i.e. $F_{s.o.} = 0$, and use the same well depth, $V_0 = -47.717$ MeV, for all channels, which gives the correct proton separation energy for the p-wave ground state. We also ignore relativistic effects (i.e. $\gamma = 1$ in Subsection 3.3), and use straight-line trajectories, without any correction for Coulomb orbits.

We choose again in this section a ^{8}B beam impinging on a lead target at 46.5 MeV/u. The proton is initially in the ground state and the time evolution is followed numerically over the time interval for which the projectile–target distance is less than 300 fm. This distance is still larger than the adiabatic distance for a 0.3 MeV excitation (viz. $\hbar v/\Delta E = 200$ fm), so our calculation covers the most import part of the interaction with the target. The calculational procedure is described in Ref. [20], where the Coulomb dissociation of an s-wave neutron halo was studied. For a p-wave proton halo one has to repeat the calculation three times, corresponding to the three different m-substates of the ground state. Moreover, in order to extract the asymptotic momentum distribution, it is important to project the final state wave function on exact continuum wave functions for the proton-core Hamiltonian. The point is that it is not very economical to follow the time evolution until the (relatively slow) protons have left the influence of the Coulomb field from the core.

Some results of higher-order calculations of the Coulomb dissociation of ^{8}B have already been reported. Typel and Baur [15] performed a perturbation expansion to second order in the Coulomb field from the target and made use of a closure approximation to sum over intermediate states in second-order processes. Bertulani [23] performed dynamical calculations similar to ours and Ref. [20] but his calculations were based on the E1 field alone. We are here mostly interested in the combined effect of the E1 and E2 fields. In this connection it is important to realize that the E2 field has a much stronger influence on the Coulomb dissociation of ^{8}B than it has in the case of a neutron halo [20] simply because the effective quadrupole charge, Eq. (2.3), is much larger for protons.

In order to assess the influence of higher-order processes in the Coulomb field from the target, we compare the results of dynamical calculations with the results of first-order perturbation theory. The E1 strength distribution we obtain with the simplified single-particle model described above is almost identical to that shown in Fig. 1. The E2 strength is weaker at the maximum (about 18%), partly because the p-wave resonance near 0.6 MeV has now disappeared. Apart from that, we expect that our calculations will show the most important qualitative features of higher-order dynamical processes.

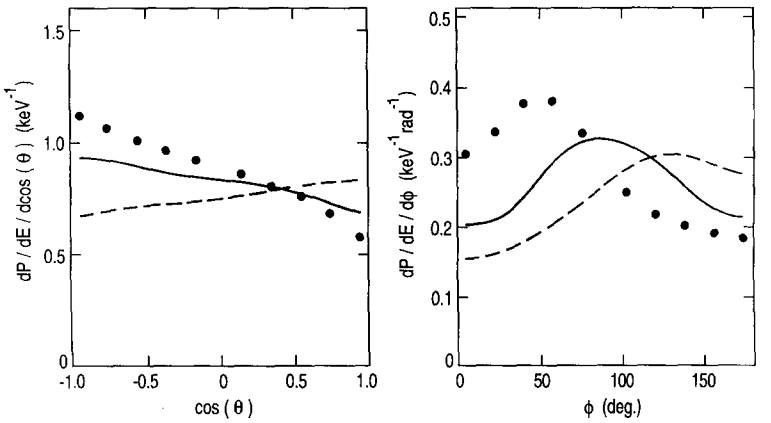

Fig. 9. Angular distributions of protons obtained at an impact parameter of 40 fm with respect to a lead nucleus and a beam energy of 46.5 MeV/u. Distributions in $\cos\theta$ and in the azimuthal angle ϕ are shown separately, for a final state kinetic energy of 0.6 MeV. The solid points are the results obtained from the E1+E2 interference in first-order perturbation theory. The curves are the results of dynamical calculations which are based on the E1 field alone (dashed curves) and on the combined effect of the E1+E2 Coulomb fields from the target (solid curves).

6.1. Angular distributions

A characteristic example on angular distributions of protons in the rest frame of ^{8}B is shown in Fig. 9, at an impact parameter of 40 fm and a final state kinetic energy of 0.6 MeV. The solid points are the result of the E1+E2 interference obtained in first-order perturbation theory and they show a pattern similar to Fig. 5. The solid curve is the result of the dynamical calculation which includes the monopole, dipole and quadrupole Coulomb fields from the target, and we see that the asymmetries are reduced compared to first-order perturbation theory.

In order to understand this reduction we repeated the dynamical calculation with the dipole field alone. This is shown by the dashed curves in Fig. 9 and they have an asymmetry opposite to the result of first-order perturbation theory. One can understand this dynamical effect as due to a post-acceleration in the Coulomb (dipole) field from the target nucleus shortly after the dissociation has taken place which gives the protons an extra push in the beam direction (towards $\cos\theta = 1$) and towards $\phi = 180°$ in the transverse direction. In fact, if we change the sign of the target charge we see a 'post-deceleration' effect: the asymmetries produced by the E1 field alone become opposite to those shown by the dashed curves. The asymmetries produced by the E0+E1+E2 fields in a dynamical calculation with a negative target charge become even larger than obtained in first-order perturbation theory simply because the dynamical 'post-deceleration' effect and the E1+E2 interference will then act coherently.

Higher-order dynamical processes will also reduce the asymmetry in the longitudinal momentum distribution of ^{7}Be fragments. This is obvious from the $\cos\theta$ distributions shown in Fig. 9. A rough estimate based on this figure suggests that the slope at the center of the longitudinal momentum distribution may be reduced by about a factor

of two compared to first-order perturbation theory. This is essentially the result we obtain from detailed dynamical calculations, summing over all excitation energies and all impact parameters larger than 40 fm, at 40.1 MeV/u on a gold target. The result is shown by the dashed curve in Fig. 8. It can be compared to the solid curve which is almost identical to the first-order result we obtain using the simpler single-particle Hamiltonian that we have adopted in this section.

In order to extract the E2 component from measurements it would clearly be an advantage if one could reduce the effect of higher-order dynamical processes. This can be achieved by increasing the beam velocity, the impact parameter or by reducing the atomic charge of the target. The cost is lower yields and concerns about nuclear induced reactions. We find by investigating the sensitivity to these parameters that the $\cos\theta$ distribution, or the longitudinal momentum distribution, is the better candidate, whereas the ϕ-distribution appears to be more strongly influenced by the higher-order dynamical effects. The best way to reduce these effects, and still keeping a large asymmetry in the $\cos\theta$ distribution, is to use a lighter target, as for example a silver target. Increasing the beam energy or the impact parameter, on the other hand, would in addition also reduce the asymmetry produced by the first-order E1+E2 interference simply because the E2 excitation probability falls off faster than the E1 probability as a function of these parameters (see, for example, Fig. 3).

6.2. *Dissociation probability and decay-energy spectrum*

The dissociation probability is shown in Fig. 10 as a function of the impact parameter b. The curves show, in increasing order, the results of first-order perturbation theory for E2 and E1 transitions separately, and the sum. The symbols show in the same order the results of dynamical calculations based on the E2 and E1 fields separately, and the combined effect of the E0+E1+E2 fields. It is reassuring to see that the dynamical calculations agree with first-order perturbation theory at large impact parameters.

A peculiar feature of the higher-order dynamical effects is that the dissociation probability is smaller than obtained in first-order perturbation. Moreover, it is not additive: the sum of the dissociation probability obtained with pure E1 and E2 fields is larger than obtained by the combined effect of the E1+E2 fields. On the other hand, if one changes the sign of the atomic charge of the target nucleus one gets the opposite result, namely that the sum is smaller than the combined effect of the E1+E2 fields. These features suggest that the most dominant higher-order dynamical process is of third order in the Coulomb field from the target. Such a process is well known in atomic stopping theory under the name 'Barkas effect'. It is a dynamical polarization effect [24] and it explains the fact that the atomic stopping power of anti-protons in solids is smaller than that of protons [25]. Thus there appears to be some analogy between the Coulomb dissociation of ^{8}B and the atomic stopping of anti-protons. A quantum mechanical explanation [26] is that one can reach the same final state as in a E1 transition simply by a second-order process of E1 and E2 transitions.

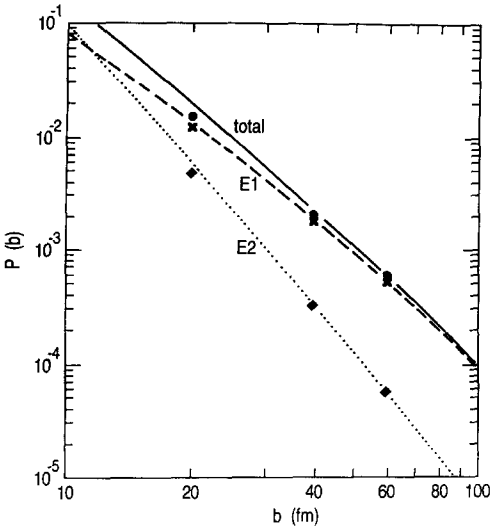

Fig. 10. Dissociation probabilities as functions of the impact parameter with respect to a lead nucleus, at 46.5 MeV/u. The curves are the results obtained in first-order perturbation theory from E2 (dotted) and E1 transitions (dashed) and the sum (solid curve). The symbols show the results, in the same order, of dynamical calculations which are based on the E2 and E1 fields separately, and the combined effect of the E1+E2 Coulomb fields from the target nucleus.

In Fig. 11 we show the decay energy spectra we obtain from perturbation theory and from dynamical calculations, both at an impact parameter of 20 fm. The dotted curves are the results of E1 transitions alone. Apparently, the higher-order dynamical effects do not modify the spectrum much in this case. This is consistent with the results of Ref. [23]. The spectrum produced by pure E2 transitions (dashed curves) is suppressed at the

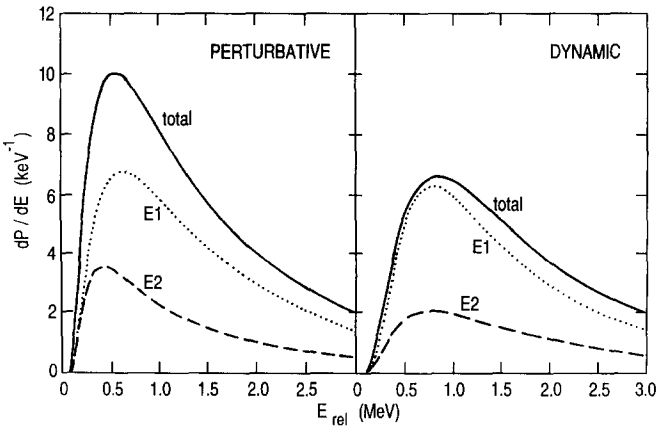

Fig. 11. Decay energy spectra from the Coulomb dissociation of ^{8}B at an impact parameter of 20 fm with respect to a lead nucleus and a beam energy of 46.5 MeV/u. The results of first-order perturbation theory and higher-order dynamical calculations are shown separately. The solid curves show the combined effect of the E1 and E2 Coulomb fields from the target. The dotted and dashed curves are the results obtained from the E1 and E2 fields separately.

maximum in the dynamical calculation compared to first-order perturbation theory. This is maybe not so surprising, according to the above discussion of the Barkas effect, since any final state reached by a single E2 transition can also be reached by two successive E2 transitions. Note that this is not possible for pure E1 transitions, consistent with the fact that the two E1 spectra do not differ much.

The combined effect of the E1 and E2 fields is shown by the solid curves in Fig. 11. They are seen to be quite different in the two approaches. Again, as we saw for the dissociation probability in Fig. 10, the combined effect of E1+E2 is not additive in the dynamical calculation, except in the tail at higher excitation energies. At the maximum, the full dynamical result is close to the maximum value obtained in first-order perturbation theory from pure E1 transitions. Thus it appears that one would exaggerate the influence of E2 transitions simply by adding the E1 and E2 contributions obtained in perturbation theory, as it was done in Ref. [2], and as we did in Fig. 4.

The apparent dynamical quenching of the contribution from E2 transitions in the peak region may explain and partly resolve the controversy that exists in the literature concerning the interpretation of the Coulomb dissociation data reported in Ref. [1]. It is at least in qualitative agreement with the recent analysis of the data which showed a surprisingly small E2 component [11]. We also note that the qualitative features of our results are different from those obtained by Typel and Baur [15]: their first- plus second-order decay energy spectra are always larger than their first-order spectra. The reason for this difference is not clear to us at present.

Let us finally mention how our results depend on the parameters of the model that we have used in this section. If we increase the radius, from 2.39 to 2.70 fm, the E1 strength increases by less than 5%, whereas the E2 strength increases from 216 to 277 $e^2\text{fm}^4$. The new E2 peak height is about the same as shown in Fig. 1 but the energy integrated strength is larger. The qualitative features of the decay energy spectrum that we obtain with the larger radius are essentially the same as those illustrated in Fig. 11: the peak height of the full dynamical calculation is much smaller than the maximum of the first-order E1+E2 result but it is close to the maximum of the first-order E1 result (it is actually 3% higher; in Fig. 11 it is 1% smaller). At higher energies, perturbation theory becomes reliable again and E2 transitions start to play a significant direct role which clearly cannot be neglected in a quantitative analysis.

Let us also mention that we always include the E0 field in the full dynamical calculations since it does appear in the multipole expansion of the Coulomb field from the target when the distance between the proton and the core is larger than the core–target distance [20]. However, its effect on the dissociation probability and the decay energy spectrum shown in Fig. 11 is quite modest.

In hindsight, it appears that the schematic model, which we have used in this section to assess the influence of higher-order processes, is probably not that poor after all. The point is that the most dominant higher-order process, the Barkas effect, is a second-order process which is due to successive E1 and E2 transitions over a wide range of intermediate energies. The fact that the model does not predict a sharp E2 resonance at 0.6 MeV is therefore not that critical. A more critical quantity is probably the total

E2 strength, say up to about 2 MeV. We are able to reproduce that strength simply by adjusting the radius parameter as discussed above. Moreover, the sharp resonance that is seen in the E2 response in Fig. 1 does not show up that clearly in the first-order decay energy spectrum shown in Fig. 4.

We shall not try to make a quantitative analysis of the Coulomb dissociation experiment [1]. It would require a careful simulation of the detection efficiency. We would also have to adjust the radius parameter of the proton-core potential (2.1) in order to reproduce the measured decay energy spectrum. Moreover, the single-particle model we have used in our dynamical calculations may not be realistic and should be improved, in particular with respect to the E2 response. Future measurements, for example of the asymmetry in longitudinal momentum distributions, will hopefully put better constraints on the E2 strength.

7. Conclusions

We have studied the effects of E2 transitions in the $^8B \rightarrow {}^7Be+p$ Coulomb dissociation on a lead target. The dissociation is dominated by E1 transitions but the interference with E2 amplitudes produces large asymmetries in the angular and momentum distributions of the two fragments. This is encouraging and suggests that it should be possible to put constraints on the E2 component from such measurements. This would then allow a more accurate extraction of the E1 component, and finally permit a more precise prediction of the $^7Be+p \rightarrow {}^8B$ radiative capture rates.

We adopted a particular single-particle model for the valence proton in ^8B. By adjusting the Woods–Saxon well depths for each channel, the model reproduces properties such as the proton separation energy and the location of known resonances. Possibly the most critical or uncertain parameter in the model is the radius of the well. The magnitude of Coulomb dissociation cross sections, and also the astrophysical S-factor, are clearly sensitive to this parameter. Our choice, which was guided by first-order perturbation theory and a recent Coulomb dissociation experiment, appears to be smaller than most of the radii commonly used.

Our predictions of asymmetries, and also of the width of the longitudinal momentum distribution, turned out to be insensitive to the radius of the Woods–Saxon well. The width of the calculated longitudinal momentum distribution of ^7Be fragments increases with increasing beam energy, and our prediction is in good agreement with a recent measurement at 1471 MeV/u on a lead target.

We have also studied the influence of higher-order dynamical processes by numerically calculating the time evolution of the wave function for the relative motion of the proton and the ^7Be core in the Coulomb field from a lead nucleus. Here we ignored spin effects and used a common Woods–Saxon potential for all single-particle channels. The associated E1 response is almost identical to that obtained from the more detailed model mentioned above but the E2 strength is somewhat weaker at the peak.

We found that higher-order processes reduce the asymmetry in the angular and mo-

mentum distributions of the fragments. The best way to eliminate these processes is to use a target with a smaller charge. Increasing the beam energy or the impact parameter would in addition also reduce the asymmetry produced by the E1+E2 interference, since the E2 amplitude falls off faster than the E1 amplitude as function of these parameters. In this connection it appears that the longitudinal momentum distribution is the better candidate, whereas the transverse distribution is more distorted by higher-order processes.

The most dominant higher-order process that affects the dissociation probability and the decay energy spectrum is of third order in the Coulomb field from the target. It is a polarization effect and it shows up because a final state, reached by a first-order E1 transition, can also be reached by second-order E1+E2 transitions. This effect is well known in atomic stopping theory where it explains the fact that the stopping power of anti-protons is smaller than that of protons. In this respect there appears to be some similarity between the Coulomb dissociation of ^{8}B and the stopping of anti-protons. Thus the dissociation probability obtained in the dynamical calculation is reduced compared to first-order perturbation theory.

Higher-order dynamical effects are clearly largest for high-Z targets, at small impact parameters and low beam energies. We investigated the decay energy spectrum in a particular case which is relevant to the recent measurement by Motobayashi et al. [1]. We found that the spectrum obtained from E1 transitions alone is almost the same in the dynamical calculation and in first-order perturbation theory. Including both E1 and E2 transitions we found that the peak height is reduced compared to the result of first-order E1 and E2 transitions but it is close to the value obtained from first-order E1 transitions alone. This result explains and partly resolves the recent controversy concerning the strength of E2 transitions in the Coulomb dissociation of ^{8}B. The strength may be there but its effect at the peak of the spectrum is apparently quenched by higher-order processes.

Acknowledgements

We are grateful to Dieter Kurath for valuable discussions. This work was supported by the US Department of Energy, Nuclear Physics Division, under Contracts W-31-109-ENG-38 and DE-FG-06-90ER-40561.

Appendix A. E1+E2 interference in angular distributions

The general expression for the angular distribution is rather complicated. It is therefore useful to study a simple case, where the interference pattern can be seen directly from an analytic expression. An example is the electric excitation of a nucleon bound in an s-wave to a core that has zero spin. Moreover, let us ignore spin–orbit effects, and set the Coulomb and nuclear fields to zero in the final state. We obtain in this case, after

inserting Eq. (3.4) into (4.1), the following expression for the final state wave function in momentum space:

$$\psi^{(f)}(k,b) = \frac{-i}{k}\sum_{\lambda\mu} F_{\lambda\mu}\langle\lambda\mu|\mathcal{M}_{\lambda\mu}|00\rangle(-i)^{\lambda}Y_{\lambda\mu}(\hat{k})$$
$$= \frac{-i}{k\sqrt{4\pi}}\sum_{\lambda\mu} F_{\lambda\mu}M_{\lambda}(-i)^{\lambda}\mathcal{D}^{\lambda}_{\mu 0}(\hat{k}). \tag{A.1}$$

Here $(-i)^{\lambda}$ is the phase shift factor due to the centrifugal potential, and M_{λ} in the last expression denotes the reduced matrix element.

From this expression one can easily derive an angular distribution which has exactly the form given in Eq. (4.3a). The A-functions, Eq. (4.3b), that one obtains in this case are

$$A^{\Lambda}_{\lambda_1\lambda_2}(k) = \frac{2\Lambda+1}{2\lambda_2+1}\langle\lambda_1 0\Lambda 0|\lambda_2 0\rangle M_{\lambda_1}M^{*}_{\lambda_2}\, i^{\lambda_2-\lambda_1}. \tag{A.2}$$

They clearly fulfill the relation (4.4) since $\lambda_1+\Lambda-\lambda_2$ is even. The simple relationship between A-functions and reduced matrix elements that one has in this case can be used as a test case in numerical calculations. Let us now look at the angular distribution in more detail.

The F-factors for electric transitions, Eq. (3.5), have a simple phase factor which we can extract and insert into (A.1). This leads to the distribution

$$\frac{dP(k,b)}{dk\,d\Omega} = |\Psi^{(f)}(k,b)|^2 = \frac{1}{4\pi}\left|\sum_{\lambda\mu} i^{\mu}\, F_{\lambda\mu}\, M_{\lambda}\, \mathcal{D}^{\lambda}_{\mu 0}(\hat{k})\right|^2, \tag{A.3}$$

where the F-factors from now on denote the absolute value of (3.5). For E1 and E2 transitions this gives

$$\frac{dP(k,b)}{dk\,d\Omega} = \frac{1}{4\pi}\left|M_1F_{10}\mathcal{D}^{1}_{00} + M_2\left(F_{20}\mathcal{D}^{2}_{00} - 2F_{22}\mathrm{Re}(\mathcal{D}^{2}_{20})\right)\right|^2$$
$$+\frac{4}{4\pi}\left|M_1F_{11}\mathrm{Re}(\mathcal{D}^{1}_{10}) + M_2F_{21}\mathrm{Re}(\mathcal{D}^{2}_{10})\right|^2, \tag{A.4}$$

and inserting the $\mathcal{D}$-functions we obtain

$$\frac{dP(k,b)}{dk\,d\Omega} = \frac{1}{4\pi}\left|M_1F_{10}\cos\theta + M_2\left(F_{20}P_2(\cos\theta) - F_{22}\sqrt{\tfrac{3}{2}}\sin^2\theta\cos 2\phi\right)\right|^2$$
$$+\frac{2}{4\pi}\left|M_1F_{11} + \sqrt{3}M_2F_{21}\cos\theta\right|^2\sin^2\theta\cos^2\phi. \tag{A.5}$$

This expression has been derived for target excitations. The coordinate system has its origin at the target, with the projectile moving in the positive direction of the z-axis, and the x-axis is in the scattering plane, pointing towards the projectile trajectory.

The formula (A.5) shows a clear interference pattern. The reduced matrix elements are both positive for a proton halo at low excitations near threshold. Thus, if we

integrate over the ϕ-angle, we obtain an enhancement for positive values of $\cos\theta$, and a reduction for negative values. This corresponds to the physical behavior that a repulsive field moving in a certain direction accelerates particles in the direction of motion.

The distribution (A.5) is symmetric around 90° as a function of ϕ. This symmetry is broken when the final state interaction and phase shifts are included. The Coulomb phase shift is particularly important, as discussed in Subsection 5.1.

Appendix B. Angular distributions for dipole excitations

The angular distribution generated by dipole excitations has a strong dependence upon the initial orbital angular momentum. We illustrate this point by comparing the distributions one obtains for initial s- and p-waves and limit the discussion to longitudinal dipole excitations. According to Eq. (4.7), this distribution is (put $\lambda_1 = \lambda_2 = 1$ and $\mu_1 = \mu_2 = 0$),

$$\left.\frac{dP}{dk\,d\Omega}\right|_{\mu=0} = \frac{F_{10}^2}{4\pi}\left(A_{11}^0 - \sqrt{\tfrac{2}{5}}\,A_{11}^2\,P_2(\cos\theta)\right). \tag{B.1}$$

The distribution for transverse dipole excitations is given by a similar expression,

$$\left.\frac{dP}{dk\,d\Omega}\right|_{\mu=\pm1} = 2\frac{F_{11}^2}{4\pi}\left(A_{11}^0 - \sqrt{\tfrac{2}{5}}\,A_{11}^2\,P_2(\cos\theta_x)\right), \tag{B.2}$$

where the angle θ_x is measured from the x-axis, which is the symmetry axis for the transverse dipole field.

In the following we ignore for simplicity the spin–orbit splitting and the spin of the core. The C-coefficients (cf. Eq. (4.3c)) one obtains in this case are

$$C_{1,2}^{\Lambda} = \frac{(2\Lambda+1)^2\langle\ell_1 0\Lambda 0|\ell_2 0\rangle}{(2\ell_0+1)(2\ell_2+1)(\lambda_2+1)} \times \sum_{\mu m_0 m}\langle\lambda_1\mu\Lambda 0|\lambda_2\mu\rangle\langle\ell_0 m_0\lambda_1\mu|\ell_1 m\rangle\langle\ell_0 m_0\lambda_2\mu|\ell_2 m\rangle\langle\ell_1 m\Lambda 0|\ell_2 m\rangle. \tag{B.3}$$

If the initial state is an s-wave one finds that the A-functions, Eq. (4.3b), are

$$A_{11}^0 = \tfrac{1}{3}M_p^2, \qquad A_{11}^2 = \frac{-\sqrt{10}}{3}M_p^2. \tag{B.4}$$

They are here expressed in terms of the reduced matrix element M_p to continuum p-waves. Inserting (B.4) into (B.1) one now obtains the familiar expression

$$\left.\frac{dP}{dk\,d\Omega}\right|_{\mu=0}^{(s)} = \frac{F_{10}^2}{4\pi}\,\frac{M_p^2}{3}\left(1+2P_2(\cos\theta)\right) = \frac{F_{10}^2}{4\pi}M_p^2\cos^2\theta. \tag{B.5}$$

If the initial state is a p-wave, then there are two reduced matrix elements, M_s and M_d, associated with the final state s- and d-waves, respectively, and the A-functions become

$$A^0_{11} = \tfrac{1}{9}\left(M_s^2 + M_d^2\right), \qquad A^2_{11} = \tfrac{1}{9}\left(-\sqrt{\tfrac{5}{2}}M_d^2 + 2\sqrt{5}M_sM_d\cos(\delta_s - \delta_d)\right). \quad \text{(B.6)}$$

This gives the angular distribution

$$\left.\frac{dP}{dk\,d\Omega}\right|^{(p)}_{\mu=0} = \frac{F^2_{10}}{36\pi}\left[M_s^2 + M_d^2 + \left(M_d^2 - 2\sqrt{2}M_sM_d\cos(\delta_s - \delta_d)\right)P_2(\cos\theta)\right]. \quad \text{(B.7)}$$

This distribution is essentially spherical at low excitation energies where s-wave final states dominate. When d-waves dominate, the relative weight of the P_2 term is only half of the value one has for an initial s-wave, cf. Eq. (B.5). When both s- and d-waves are important in the final state, phase-shift differences between the two waves may reduce the significance of the P_2 term. This explains why the angular distribution generated by dipole transitions is much closer to being spherical when the initial state is a p-wave than when it is an s-wave.

References

[1] T. Motobayashi et al., Phys. Rev. Lett. 73 (1994) 2680.
[2] K. Langanke and T.D. Shoppa, Phys. Rev. C 49 (1994) 1771.
[3] H. Esbensen and G.F. Bertsch, Phys. Lett. B 359 (1995) 13.
[4] D. Kurath, (private communication)
[5] R.G.H. Robertson, Phys. Rev. C 7 (1973) 543.
[6] H. Esbensen, B.A. Brown and H. Sagawa, Phys. Rev. C 51 (1995) 1274.
[7] F. Ajzenberg-Selove, Nucl. Phys. A 490 (1988) 103.
[8] A. Bohr and B.R. Mottelson, Nuclear Structure, vol. I (Benjamin, New York, 1969).
[9] A.R. Edmonds, Angular Momentum in Quantum Mechanics (Princeton Univ. Press, Princeton, 1960).
[10] G. Taubes, Science 266 (1994) 1157.
[11] M. Gai and C. A. Bertulani, Phys. Rev. C 52 (1995) 1706.
[12] G. Baur, C.A. Bertulani and H. Rebel, Nucl. Phys. A 458 (1986) 188.
[13] B.W. Filippone, A.J. Elwyn, C.N. Davids and D.D. Koetke, Phys. Rev. C 28 (1983) 2222.
[14] K.H. Kim, M.H. Park and B.T. Kim, Phys. Rev. C 35 (1987) 363.
[15] S. Typel and G. Baur, Phys. Rev. C 50 (1994) 2104.
[16] A. Winther and K. Alder, Nucl. Phys. A 319 (1979) 518.
[17] H. Esbensen, Phys. Rev. C 44 (1991) 440.
[18] D. Varshalovich, A. Moskalev and V. Khersonskii, Quantum Theory of Angular Momentum (World Scientific, Singapore, 1988) p. 459, Eq. (21).
[19] T. Nakamura et al., Phys. Lett. B 331 (1994) 206.
[20] H. Esbensen, G.F. Bertsch and C.A. Bertulani, Nucl. Phys. A 581 (1995) 107.
[21] W. Schwab et al., Z. Phys. A 350 (1995) 283.
[22] J.H. Kelley et al., (to be published).
[23] C.A. Bertulani, Nucl. Phys. A 587 (1995) 318.
[24] J. Lindhard, Nucl. Instr. Methods 132 (1976) 1.
[25] L.H. Andersen et al., Phys. Rev. Lett. 62 (1989) 1731.
[26] K.W. Hill and E. Merzbacher, Phys. Rev. A 5 (1974) 156.